ACS APPLIED MATERIALS & INTERFACES

Research Article

www.acsami.org

New Synthesis of a Foamlike Fe_3O_4/C Composite via a Self-Expanding Process and Its Electrochemical Performance as Anode Material for Lithium-Ion Batteries

Feng Wu, Rong Huang, Daobin Mu,* Borong Wu, and Shi Chen

Beijing Key Laboratory of Environmental Science and Engineering, School of Chemical Engineering and Environment, Beijing Institute of Technology, Beijing 100081, China

ABSTRACT: A novel foamlike Fe_3O_4/C composite is prepared via a sol–gel type method with gelatin as the carbon source and ferric nitrate as the iron source, following a postannealing treatment. Its lithium storage properties as anode material for a lithium-ion battery are thoroughly investigated in this work. With the interaction between ferric nitrate and gelatin, the foamlike architecture is attained through a unique self-expanding process. The Fe_3O_4/C composite possesses abundant porous structure along with highly dispersed Fe_3O_4 nanocrystal embedment in the carbon matrix. In the constructed architecture, the 3D porous network property ensures electrolyte accessibility; meanwhile, nanosized Fe_3O_4 promotes lithiation/delithiation, owing to numerous active sites, large electrolyte contact area, and a short lithium ion diffusion path. As a result, this Fe_3O_4/C composite electrode demonstrates an excellent cycling stability with a reversible capacity of 1008 mA h g^{-1} over 400 cycles at 0.2C (1C = 1000 mA g^{-1}), as well as a superior rate performance with reversible capacity of 660 and 580 mA h g^{-1} at 3C and 5C, respectively.

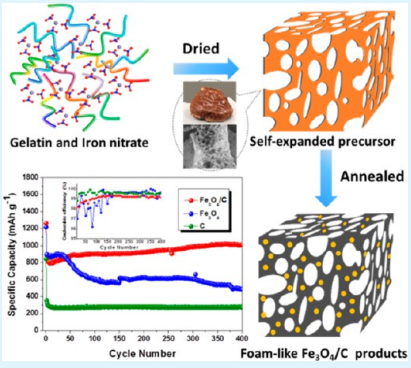

KEYWORDS: *magnetite, foamlike structure, self-expanding process, anode, lithium-ion batteries*

INTRODUCTION

Rechargeable lithium-ion batteries (LIBs), as the most popular power source or energy storage system, have been widely used in portable electronic devices, electric vehicles, electric grids, etc.[1−3] With increasing market demands, urgent challenges to develop high energy and power battery systems have been emerging. As a crucial part of LIBs, the commercial graphite anode has an inherent shortage of capacity. The graphite theoretical value of 372 mA h g^{-1} is inadequate to meet the growing requirements of high energy batteries.[4,5] Among various alternative anode materials, magnetite (Fe_3O_4) shows attractive merits as a potential candidate due to its high theoretical capacity (926 mA h g^{-1}), ecofriendliness, natural abundance, low cost, and high electronic conductivity (2×10^4 S m^{-1}).[6−8] Despite these advantages, the anode material easily suffers from sluggish kinetics in conversion reaction processes. Furthermore, severe volume variation (200%) and particle agglomeration occur during repeated lithiation/delithiation reactions, resulting in electrode degradation over several charge/discharge cycles. Consequently, the anode material is not satisfactory in capacity retention and rate capability, which also hinders its practical application.[9,10]

To solve these issues, one possible solution is to employ nanosized Fe_3O_4 with various morphologies and structures, such as nanoparticles,[11] nanorods,[12] nanowires,[13] nanorings,[14] and hollow nanostructure,[15] aimed at relieving the strain caused by lithium insertion/extraction, shortening the path length for Li^+ transport, and increasing access to electrolyte. Nevertheless, the nanoscale particles with large surface area easily agglomerate to form secondary aggregates, leading to debasing the electrode stability. Another possible solution is the combination of nanosized Fe_3O_4 with multifunctional carbon materials.[16−19] For example, metal oxides have been coated with a thin carbon layer,[20] supported with a carbon substrate, and embedded in a porous carbon matrix.[21−23] The carbonaceous material acts as a buffer layer, alleviating the volume variation of active particles upon cycling, and as a conductive matrix for electron transfer. Additionally, it can provide active sites for crystal growth and prevent particle agglomeration. Various kinds of nanostructured carbonaceous materials, such as graphene, carbon nanotubes (CNTs), and porous carbon including mesocellular carbon, carbon foam, and ordered mesoporous carbon (CMK-3), have been used as hosts because of their highly specific surface and high loading capacity for active materials.[24−28] However, most of the host materials need a complicated preparation process with tedious steps under severe conditions. In addition, to obtain the composites, extra processes are further required to combine hosts with active materials, for instance, solvothermal method, thermal decomposition, thermal evaporation, etc. Moreover, some problems still exist for the Fe_3O_4 anode, such as low Coulombic efficiency, unsatisfactory cycling life and rate capacity, and in particular the links with the material architecture.

Received: August 7, 2014
Accepted: October 6, 2014
Published: October 6, 2014

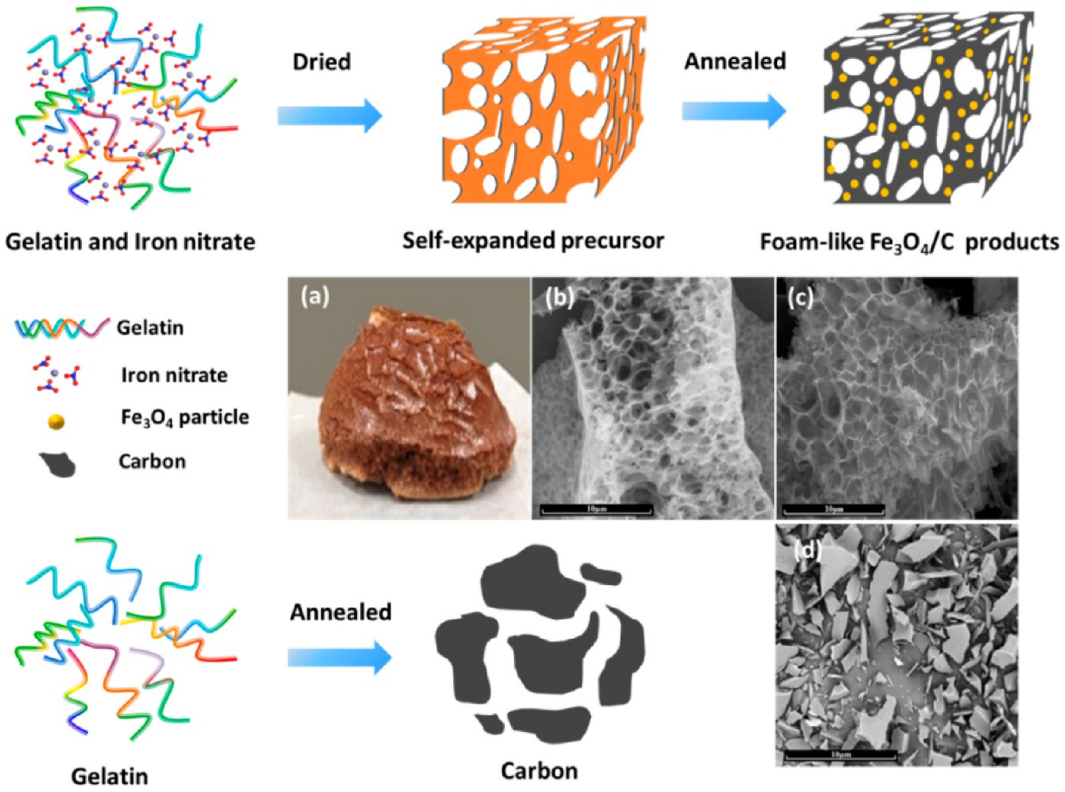

Figure 1. Schematic illustration for the formation of the foamlike Fe_3O_4/C composite and the block carbon material. (a) Photograph of solid precursor. SEM image of (b) self-expanded precursor, (c) Fe_3O_4/C composite, and (d) block carbon.

In this study, we reported the synthesis of a novel foamlike Fe_3O_4/C composite through a unique self-expanding process. With the interaction between ferrous nitrate and gelatin, the foam structure was achieved. During the in situ growth process, the fine Fe_3O_4 crystals could be homogeneously dispersed and embedded in the carbon matrix, which effectively confined active particle size and avoided nanoparticle agglomeration. This simple method, based on biomass and low cost precursors, offered a green and low cost new approach to prepare the Fe_3O_4/C composites. Herein the synthesis strategy, surface morphology, microstructure, and chemical composition of the as-prepared Fe_3O_4/C composite were examined in detail. As anode material, its lithium storage properties and reaction mechanism were thoroughly investigated, together with bare Fe_3O_4 and pure carbon anodes for comparison.

EXPERIMENTAL SECTION

Materials Synthesis. The reagents were obtained from commercial sources and used without further purification. Typically, 10 g of gelatin was dissolved in 90 mL of hot deionized water under continuous stirring to obtain a slightly yellow solution A. Solution B was prepared by dissolving 10 mmol of $Fe(NO_3)_3{\cdot}9H_2O$ in 40 mL of deionized water. Solution B was then added to 20 mL of solution A dropwise to make a viscous mixed solution. With vigorous stirring and continuous heating at 60 °C, the mixed solution changed into a brown, sticky, toffeelike gel. Then further drying at 80 °C induced a foamlike solid formation by a self-expanding process. Next the product was annealed at 500 °C under an argon environment for 2 h to obtain a Fe_3O_4/C composite.

To gain pure carbon material, the as-prepared Fe_3O_4/C composite was etched by 0.1 M HCl with stirring for 24 h. The powders were collected by centrifugation, washed with deionized water, and dried at 60 °C.

In comparison, bare Fe_3O_4 particles were prepared according to the literature procedure.[29] A 20 mmol amount of $Fe(NO_3)_3{\cdot}9H_2O$ was added to 25 mL of ethylene glycol (EG) under stirring to produce a homogeneous solution. The solution was continuously heated at 80 °C until a gel formed. Finally, the gel was annealed at 600 °C for 10 h to yield bare Fe_3O_4 material.

Materials Characterization. The sample was characterized by X-ray diffraction (XRD; Rigaku Ultima IV-185) with a Cu Kα radiation source (scan rate: 2° min^{-1}, scan range: 10°−80°) and by Raman spectroscopy (Renishaw RM 2000) with 632.8 nm excitation from a He−Ne laser. The morphology of the sample was analyzed using a field-emission scanning electron microscope (FE-SEM QUANTA 6000) equipped with an energy-dispersive X-ray (EDX) detector. Transmission electron microscopy (TEM) and high-resolution transmission electron microscopy (HRTEM) analysis was carried out on a JEM-2010 instrument. Thermogravimetry (TG) analysis of the sample was carried out at a ramping rate of 10 °C min^{-1} from room temperature to 800 °C in air atmosphere (Seiko TG/DTA6300). The elemental states in the composite were revealed with an X-ray photoelectron spectrometer (XPS). The measurement was conducted on a PHI QUANTERA-II SXM system, using a monochromatized Mg Kα radiation source.

Electrochemical Test. Electrochemical tests were conducted on a CR2025-type coin cell. The working electrode was prepared by mixing 80 wt % as-prepared active material, 10 wt % carbon black (Super P) as conductive additive, and 10 wt % polyvinylidene fluoride (PVDF) as binder in *N*-methylpyrrolidinone (NMP) to form a viscous slurry. The slurry was then coated onto a Cu foil and dried in an oven at 100 °C overnight. The dried electrode was cut into a disk with a diameter of 11 mm. The active material per electrode is about 2−2.2 mg cm^{-2}. The cell was assembled in an argon glovebox, using a lithium sheet as counter and reference electrodes, 1 mol L^{-1} $LiPF_6$/DMC + DEC + EC (1:1:1 in volume) as electrolyte, and a Celgard 2300 membrane as a separator. Galvanostatic charge/discharge tests were carried out on a LAND CT2001A battery testing system between 0.005 and 3 V at various current densities (0.2C, 0.5C, 1C, 2C, 3C, and 5C; 1C = 1000

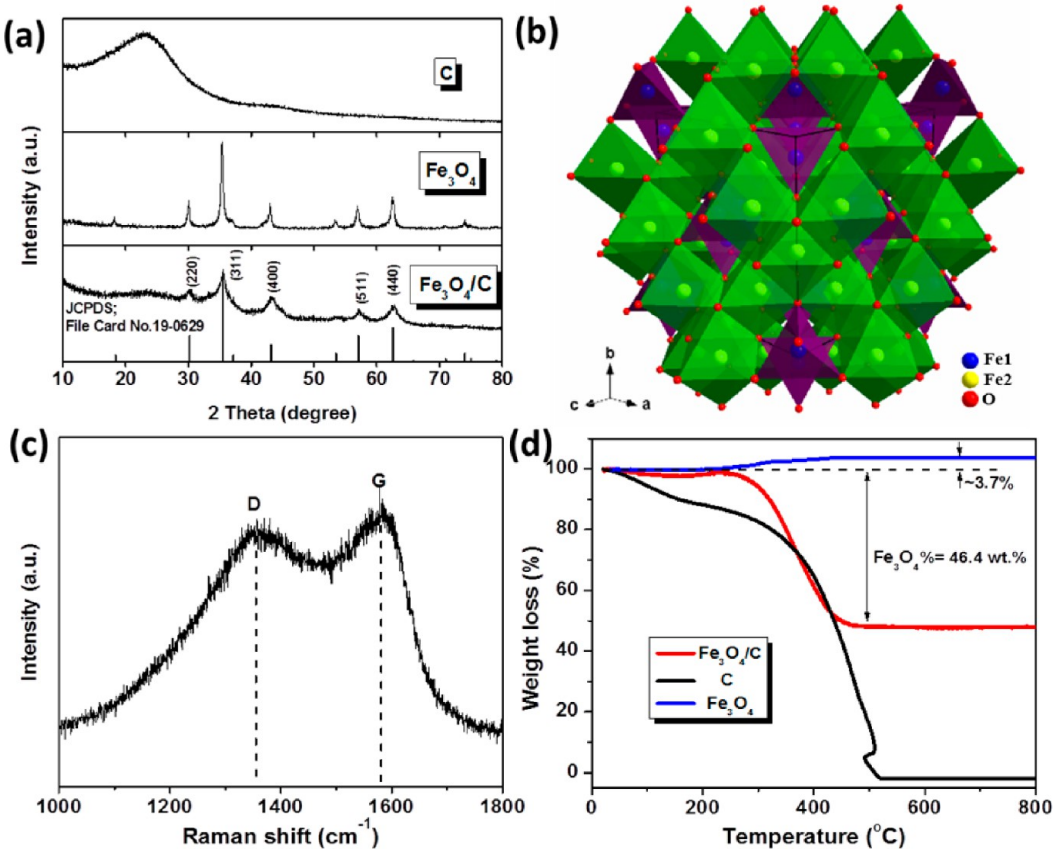

Figure 2. (a) X-ray diffraction patterns of Fe_3O_4, carbon, and the Fe_3O_4/C composite. (b) The crystal structure of the unit cell of Fe_3O_4. (c) Raman spectrum of the Fe_3O_4/C composite. (d) TGA profiles of Fe_3O_4, carbon, and the Fe_3O_4/C composite.

mA g^{-1}). Cyclic voltammetry (CV) of the electrode was recorded from 0.005 to 3 V at scan rates of 0.1, 0.2, 0.5, 1, 2, 3, 5 mV s^{-1}. Electrochemical impedance spectroscopy (EIS) measurement was performed at a frequency range from 100 kHz to 10 mHz with a perturbation amplitude of 5 mV. Both CV and EIS measurements were conducted on a CHI 660D electrochemical workstation. The potentials mentioned in this study refer to the Li/Li^+ redox couple.

RESULTS AND DISCUSSION

The self-expanding process to prepare the foamlike Fe_3O_4/C composite is schematically illustrated in Figure 1. Gelatin, as a biopolymer, is composed of glycine, proline, hydroxyproline, and other amino acids. The composite may provide sites for metal cation binding.[30] In the synthesis process, ferric nitrate and gelatin were mixed together under heating to form a viscous gel, leading to strong binding between Fe^{3+} and the functional groups of gelatin, conducing a homogeneous dispersion of metal salt in the mixture. The interaction between biopolymers and metal cations can form an interpenetrating covalent network. Upon drying, the gel self-expands to be a brittle and loose solid precursor, as shown in Figure 1a. Meanwhile, a foamlike porous structure is formed, as shown in the SEM image (Figure 1b). The process is caused by the production of gas bubbles due to the oxidation of gelatin with ferric nitrate, as confirmed by Schnepp et al.[31] When $FeCl_3$ was used as reactant, no expansion phenomenon appeared along with the production of hard solid precursor. Therefore, we guess that the nitrate substance takes a predominant role in causing the self-expanding process. The strongly cross-linked superstructure ensured the structural stability of the expanded foam. Importantly, the unique constructure remains unchanged even after a postannealing treatment, as shown in Figure 1c, during which the solid precursor is carbonized, together with ferrous oxide attained in situ with the fine crystal size based on the template nucleation.[32,33] The SEM morphology of the as-prepared composite presents a foamlike structure with abundant porous channels. These widely dispersed pores are ~0.3−1.5 μm in diameter and interconnected to form well-defined 3D networks. Comparatively, no expansion occurs when only pure gelatin is treated under the same condition, and just a block carbon is obtained (Figure 1d). This result further proves that the coordinated interaction between the ferric nitrate and gelatin seems to play an important role in the structure formation.

Figure 2a shows the XRD patterns of the as-prepared pure carbon, bare Fe_3O_4, and foamlike Fe_3O_4/C composite. The position and relative intensities of all diffraction peaks in both Fe_3O_4 and Fe_3O_4/C samples could be well indexed to the cubic phase of magnetite with $Fd\bar{3}m$ space group (Fe_3O_4: JCPDS no. 19-0629). According to the simulated result (Figure 2b), Fe_3O_4 possesses a spinel type crystal structure with two kinds of cation sites existing in the crystal. Typically, Fe1 occupies the tetrahedrally coordinated 8a sites and is coordinated as a FeO_4 tetrahedron, while Fe2 occupies the octahedrally coordinated 16d sites and is coordinated as a FeO_6 octahedron. Fe1 is normally assigned with a charge state 3+. Fe2 is always assigned with charge states 2+ and 3+ in equal numbers.[34] The formula of magnetite (Fe_3O_4) contains two 3+ and one 2+ iron ions, corresponding to an eight-electron transfer during the conversion reaction process. Accordingly, the formula of Fe_3O_4

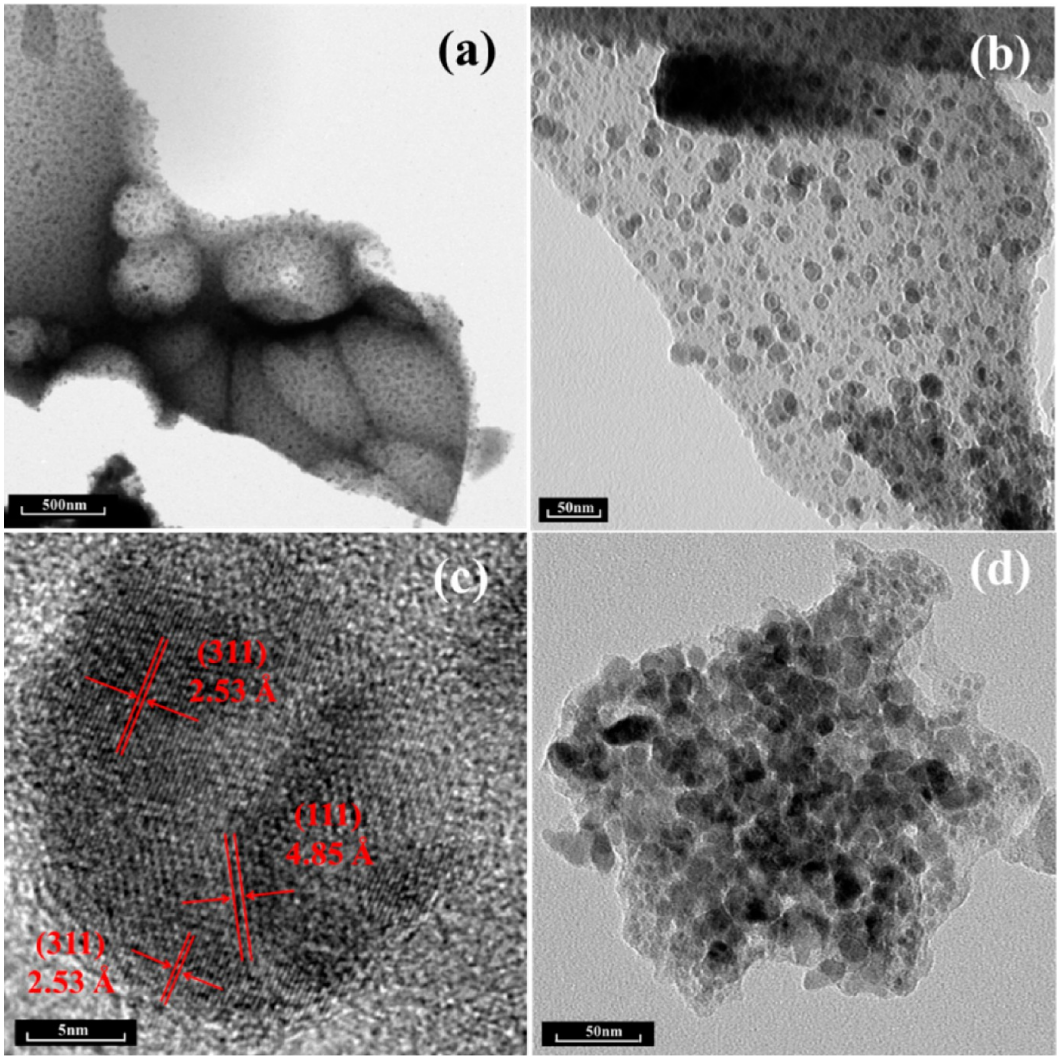

Figure 3. (a, b) TEM images of the Fe_3O_4/C composite. (c) HRTEM image of the Fe_3O_4/C composite. (d) TEM images of bare Fe_3O_4.

can accommodate eight Li ions, resulting in a theoretical specific capacity of 926 mA h g^{-1}. The relatively narrow and sharp diffraction peaks suggest a highly crystalline nature for the obtained bare Fe_3O_4. By contrast, the weak and broad peaks indicate that the Fe_3O_4 particles in the as-prepared Fe_3O_4/C composite are of nanometer size and not well crystallized. From Scherrer's formula, the average crystallite sizes of the bare Fe_3O_4 particle and the Fe_3O_4 in the composite are estimated to be 20 and 15 nm, respectively. The obviously high background of Fe_3O_4/C in the XRD pattern indicates the presence of amorphous carbon.[35] To confirm this view further, the Fe_3O_4/C composite was etched with HCl to remove Fe_3O_4. The broad diffraction peak (Figure 2a) in the 20−30° range of the remaining material can be ascribed to carbon species, which accords well with reports in the literature.[36,37] In addition, the XRD result implies that the carbon matrix of the composite is not highly graphitized.[38,39]

Raman spectroscopy was also carried out to study the nature of carbon species in the foamlike Fe_3O_4/C composite, as shown in Figure 2c. The recorded spectrum presents two distinct peaks at about 1357 and 1595 cm^{-1}. They correspond to the D band and G band, respectively. This result also confirms the carbonization of the gelatin precursor. The D band is associated with the A_{1g} phonon of sp^3 carbon atoms in disordered graphite, and the G band is ascribed to the in-plane vibration of sp^2 carbon atoms in the basal plane of crystalline graphite. The peak intensity ratio of D band to G band (I_D/I_G) can be used to estimate the degree of crystallinity of the carbon material. A smaller value means a higher degree of atom ordering. Here, the I_D/I_G value is calculated to be 0.91, also indicating that the carbon in the composite is partially graphitized as well,[40,41] so the electronic conductive property may be improved due to the carbon matrix.

The content of Fe_3O_4 in the composite was evaluated by thermogravimetric (TG) analysis, as shown in Figure 2d. With the heat treatment from room temperature to 800 °C under air atmosphere, the carbon can be oxidized to CO_2; Fe_3O_4 is oxidized to Fe_2O_3 ($C + O_2 \rightarrow CO_2$; $4\ Fe_3O_4 + O_2 \rightarrow 6\ Fe_2O_3$). As for bare Fe_3O_4, a weight increase of 3.7% is found, owing to its oxidation. For the Fe_3O_4/C composite, based on the remaining weight of Fe_2O_3 (48%), the original weight fraction of Fe_3O_4 is calculated as 46.4%. The total consumption of pure carbon sample indicates that Fe_3O_4 particles have been etched completely.

Figure 3a and 3b shows typical TEM images of Fe_3O_4/C composite architecture. Clearly, Fe_3O_4 crystals are homogeneously embedded in the carbon matrix. The particle size with an average diameter of ∼10−15 nm is well consistent with the

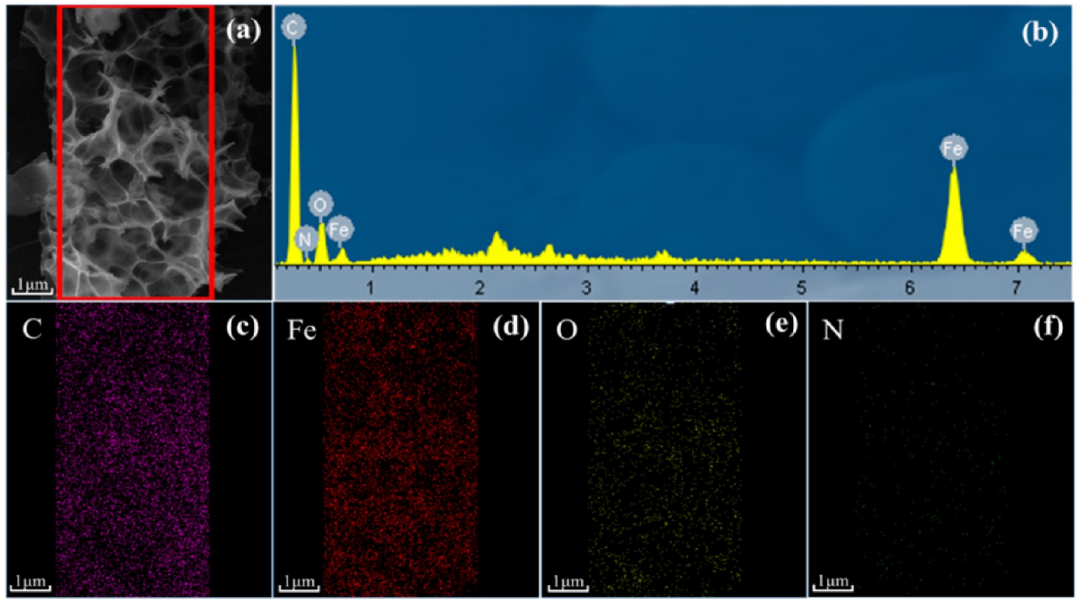

Figure 4. (a) FESEM images of the Fe_3O_4/C composite. (b) EDS spectrum of the Fe_3O_4/C composite. (c) C, (d) Fe, (e) O, and (f) N element maps corresponding to the FESEM image shown in panel a.

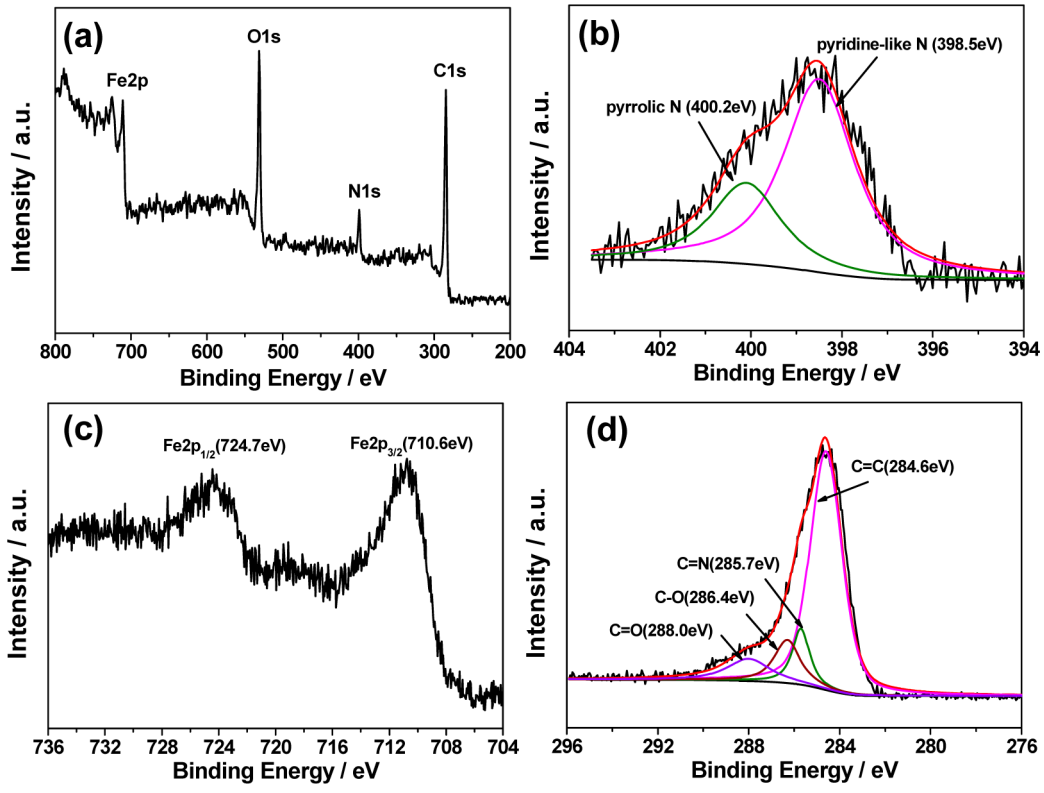

Figure 5. (a) XPS full spectra of the Fe_3O_4/C composite. High-resolution XPS spectra of (b) N 1s (c) Fe 2p, and (d) C 1s regions of the Fe_3O_4/C composite.

calculated result based on Scherrer's formula. The fine nanoparticles favor the mitigation of volume expansion/contraction during the continuous Li^+ insertion/extraction process and favor the shortening of the Li^+ transport path in the solid phase. The structure can effectively confine active seed growth, avoid particle agglomeration, and maintain a highly active surface area, providing sufficient contact between electrolyte and electrode. The HRTEM image in Figure 3c demonstrates a typical Fe_3O_4 particle with good crystalline texture. The *d*-spacings of 4.85 and 2.53 Å are in good agreement with the (111) and (311) planes, respectively. For comparison, the image of the bare Fe_3O_4 particles is displayed in Figure 3d. It shows irregular particle shapes with numerous aggregations.

According to energy-dispersive spectroscopy (EDS) elemental mapping (Figure 4), the elements of C, Fe, and O are homogeneously distributed in the detected areas. This confirms that the Fe_3O_4 nanoparticles are uniformly dispersed in the

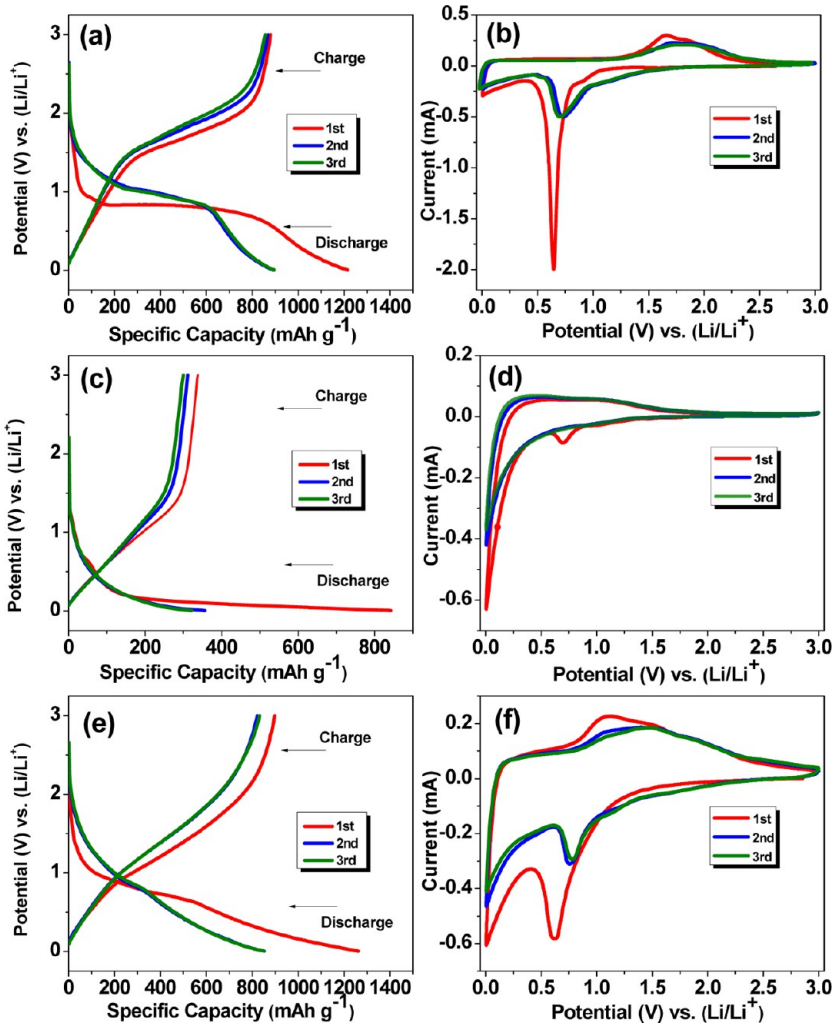

Figure 6. Galvanostatic charge/discharge profiles of (a) Fe_3O_4, (c) carbon, and (e) Fe_3O_4/C composite electrodes over the first three cycles. Cyclic voltammetry profiles of (b) Fe_3O_4, (d) carbon, and (f) Fe_3O_4/C composite electrodes at 0.1 mV s^{-1} scan rate.

carbon matrix. Accidentally, element N is also detected, as shown in Figure 4f, possibly owing to residual N species from the thermal decomposition of gelatin. It has been demonstrated that the size of the nitrogen atom is comparable to that of carbon, and its five valence electrons are available to form strong valence bonds with carbon atoms.[42−44] As proved by first-principle calculation, nitrogen atom doping could potentially produce highly localized active regions of carbon and improve the interfacial stability and electric conduction.[45] Thus, the residual N species may also make a contribution to enhance the electrochemical performance of the composite.

The presence of N species is further confirmed by X-ray photoelectron spectroscopy (XPS) analysis. As shown in Figure 5a, the main signals presented in the survey spectra are Fe 2p, O 1s, N 1s, and C 1s, indicating the presence of Fe, O, N, and C elements in the composite. Here the N 1s peak could be identified as two peaks at 400.2 and 398.5 eV, representing pyrrolic nitrogen and pyridine-like nitrogen in the carbon matrix, respectively (Figure 5b). Moreover, the nitrogen content of the composite is calculated to be 9.35 wt % according to the XPS analysis. In the enlarged range of the Fe 2p spectrum (Figure 5c), the binding energies of Fe $2p_{1/2}$ and Fe $2p_{3/2}$ are found to be 724.7 and 710.6 eV, corresponding to the spin orbit peaks of Fe_3O_4. In addition, the C 1s peak is split into four typical components: the peak at 284.6 eV represents carbon atoms in the C═C bond, reflecting the extensively delocalized sp^2-hybridized carbon; the peak at 285.7 eV reflects the structure of the C═N bond, which may originate from the substitution of the N atoms and the defects or edge of the N-doped carbon; the peaks at 286.4 and 288.0 eV are attributed to the C−O bond and C═O bond, respectively.[46,47]

Figure 6 compares the galvanostatic charge/discharge curves and the cyclic voltammetry (CV) among bare Fe_3O_4, pure carbon, and Fe_3O_4/C composite electrodes in the initial three cycles. In Figure 6, parts a, c, and e, the galvanostatic charge/discharge was tested at 200 mA g^{-1} over a potential range of 0.005−3 V. The bare Fe_3O_4 electrode exhibits a specific capacity of 1216.3 and 879.5 mA h g^{-1} in the first discharge (lithiation) and charge (delithiation) process with a Coulombic efficiency of 72.3%. A short slope from open circuit potential to 0.7 V originates from Li^+ insertion, as described in eq 1, together with the formation of a solid electrolyte interphase (SEI) film. The reaction at a long potential plateau around 0.7 V in the discharge curve makes a major contribution to the discharge capacity. It corresponds to the reduction of the oxidation state of iron to Fe^0 accompanying simultaneous amorphous Li_2O formation, as illustrated in eq 2.

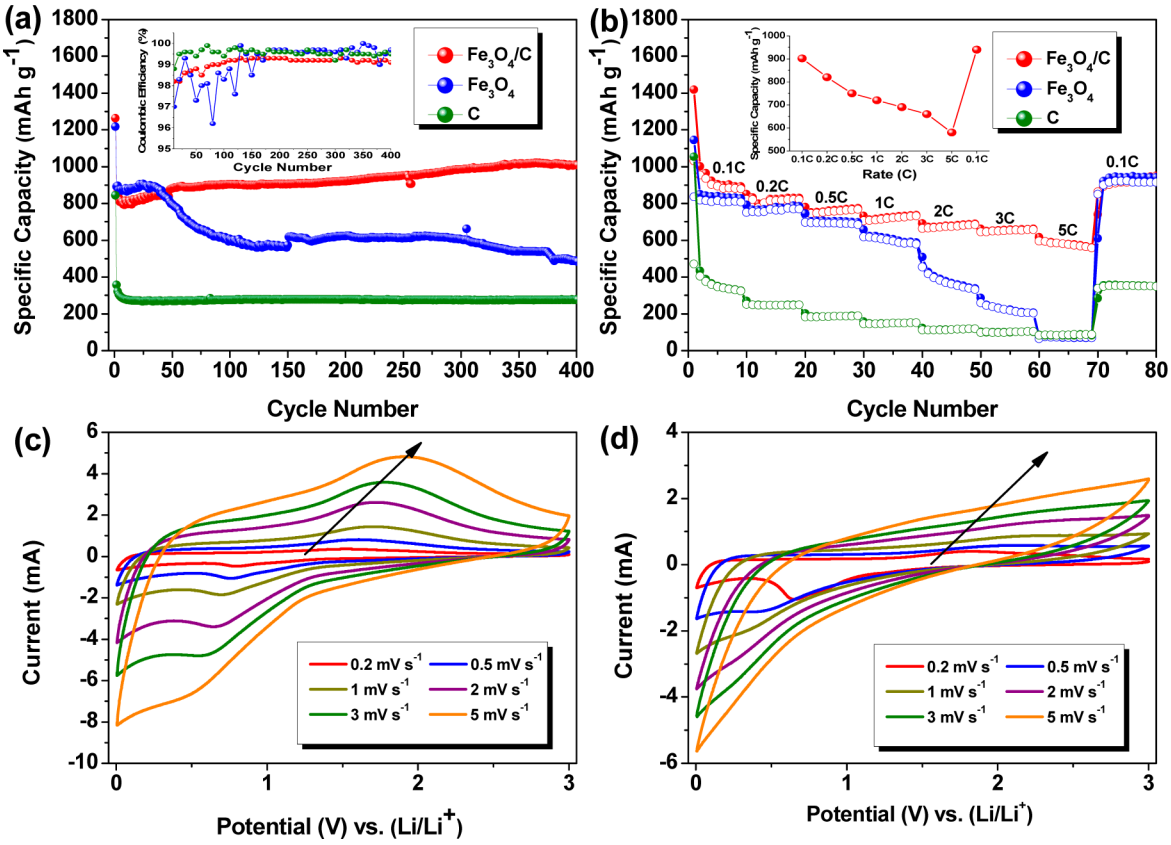

Figure 7. (a) Cycle performance of Fe_3O_4, carbon, and Fe_3O_4/C composite electrodes at current density 200 mA g^{-1} in the potential range 0.005–3.0 V. (b) Rate performance of Fe_3O_4, carbon, and Fe_3O_4/C composite electrodes at various current densities (solid symbols represent lithiation; hollow symbols represent delithiation). Cyclic voltammetry profiles of (c) Fe_3O_4/C composite electrodes (d) bare Fe_3O_4 electrodes at various scan rates.

As a comparison, the initial discharge capacity and Coulombic efficiency of the as-prepared pure carbon electrode are 843.2 mA h g^{-1} and 40.1%, respectively. A plateau near 0.1 V can be seen in the discharge curve, which may be ascribed to lithium intercalation into the carbon material (eq 3). For the Fe_3O_4/C composite electrode, it delivers capacities of 1262.5 and 898 mA h g^{-1} in the initial discharge/charge, respectively. The discharge curve shows two plateaus near 0.7 and 0.1 V, thus indicating that the discharge capacity of the composite electrode is composed of contributions from both Fe_3O_4 and carbon.

$$Fe_3O_4 + \chi Li^+ + \chi e^- \rightarrow Li_\chi Fe_3O_4 \quad (1)$$

$$Li_\chi Fe_3O_4 + (8-\chi)Li^+ + (8-\chi)e^- \rightarrow 4Li_2O + 3Fe \quad (2)$$

$$C + \chi Li^+ + \chi e^- \rightarrow Li_\chi C \quad (3)$$

Figure 6, parts b, d, and f, presents the CV profiles of Fe_3O_4, carbon, and Fe_3O_4/C composite electrodes in the potential range of 0.005 to 3.0 V at the scan rate of 0.1 mV s^{-1}. In the first cathodic scan stage (lithiation), a strong reduction peak near 0.65 V is apparently observed for both Fe_3O_4 and Fe_3O_4/C composite electrodes. It is associated with reduction of the oxidation state of iron to Fe^0, corresponding to the long discharge plateau and the reaction in eq 2. For the pure carbon and Fe_3O_4/C composite electrodes, the reduction peaks at 0.1 V reflect lithium ion intercalation in the carbon matrix (eq 3). In the anodic scan process, the wide oxidation peak of the Fe_3O_4 electrode around 1.65 V is attributed to the oxidation of Fe^0; correspondingly, the oxidation peak of the Fe_3O_4/C composite electrode is around 1.1 V. For the Fe_3O_4/C composite electrode, the fine Fe_3O_4 particles are embedded in the foamlike porous carbon matrix. The access to the electrolyte is quite sufficient compared to the pure Fe_3O_4 electrode. In addition, the hybrid carbon provides a conductive network. As a result, the composite electrode could present modified kinetic properties with lower polarization. Here a relatively small value of peak potential difference means an improvement in reaction reversibility. The oxidation peaks at ~0.1 V for both pure C and Fe_3O_4/C electrodes always indicates Li^+ deintercalation from the graphite phase ($Li_\chi C \rightarrow C + \chi\ Li^+ + \chi\ e^-$). From the second cycle onward, the peak positions, intensities, and integral areas of cathodic and anodic peaks are nearly overlapped for all three electrodes, indicating that the electrochemical reaction tends to be stable.

The cycle performance of the three electrodes is shown in Figure 7a. Obviously, the composite electrode presents a cycling stability much better than that of the bare Fe_3O_4 electrode, as well as a remarkably higher reversible capacity compared to pure carbon electrode. The composite electrode demonstrates a reversible capacity of 1008 mA h g^{-1} even up to 400 cycles, which is far higher than the value of 275.9 mA h g^{-1} for pure carbon material and 540.8 mA h g^{-1} for the bare Fe_3O_4 electrode. Furthermore, its Coulombic efficiency is maintained at ~99.2% (Figure 7a (inset)), suggesting an effectively reversible lithiation/delithiation process. Here the reversible capacity of the composite electrode gradually increases during

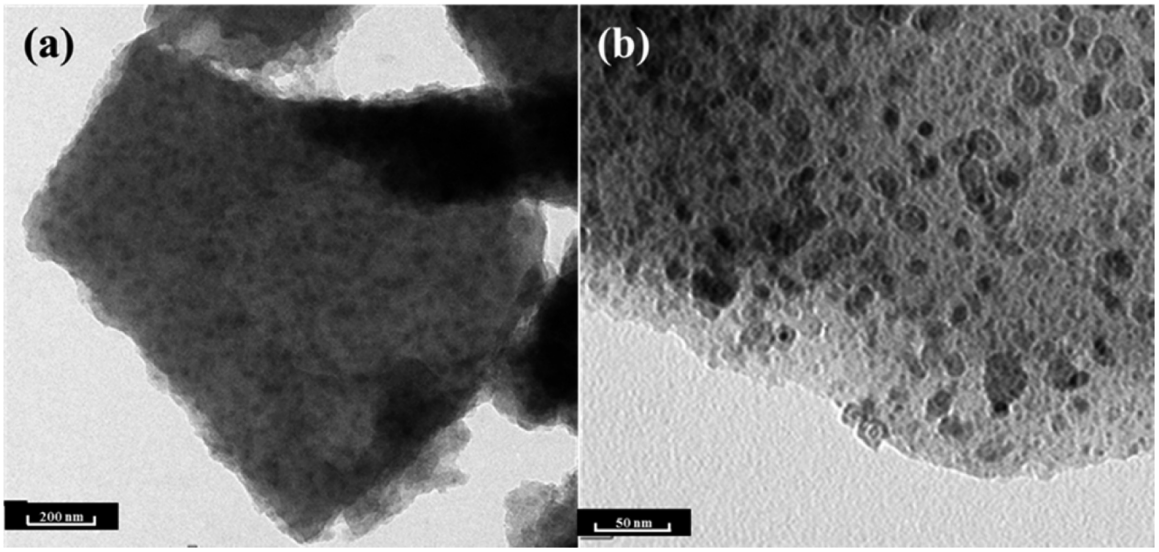

Figure 8. TEM images of Fe_3O_4/C composite after 100 cycles at (a) low and (b) high magnification.

the cycling process. This phenomenon is commonly found in both Fe-based transition metal oxides and other metal oxides, such as MnO and SnO_2. Based on previous reports, the trend of increasing reversible capacity may be attributed to the gradual improvement of lithium ion accessibility and the formation of a pseudocapacitive polymeric gellike film due to the decomposition of the electrolyte during the continuous conversion reaction process.[48−51] For the Fe_3O_4 electrode, the capacity fades after 40 cycles, which may result from structure deterioration during the continuous volume expansion/contraction. Meanwhile, the pure carbon electrode exhibits a relatively low reversible capacity but with outstanding cycle stability. So it should primarily contribute to the overall structure stability, despite a small contribution to the overall capacity of the composites.

On the basis of the unique structure characteristics, as expected, the Fe_3O_4/C composite electrode also presents a satisfying rate performance upon cycling in a step mode with different densities (Figure 7b). The inset shows the average reversible capacities of the Fe_3O_4/C composite electrode at various rates. The composite electrode delivers a reversible capacity of 690 mA h g^{-1} and 660 mA h g^{-1} when cycled at 2C (1C = 1000 mA g^{-1}) and 3C, respectively. A value of 580 mA h g^{-1} can still be retained when the current density increases to 5C. When the current density switches back to 0.1C from 5C, the specific capacity returns to 940 mA h g^{-1} again, implying the structure stability of the composite even at a high rate. In contrast, the bare Fe_3O_4 and pure carbon electrodes show relatively lower reversible capacity and rapidly fading capacity with gradually increasing current density. The CV curves of the composite and bare Fe_3O_4 electrodes at different scan rates were also examined, as shown in Figure 7c,d. The scan rate from 0.2 mV s^{-1} to 5 mV s^{-1} corresponds to the 0.25C to 6C rates approximately in terms of the estimation of scan time. In the CV curves, the cathodic and anodic peaks reflect the kinetics of lithium insertion/extraction at the electrode/electrolyte interface and the lithium diffusion.[52] With an increase in scan rate, the peaks shift toward lower and higher potentials. The redox peak potential difference increases, resulting in larger polarization. As a result, the electrode reactivity declines, leading to a degradation of rate capability and cycling performance. For the Fe_3O_4/C composite electrode, the curve still presents distinct redox peaks at a higher rate (5 mV s^{-1}). However, almost no peaks appear when the scan rate reaches 1 mV s^{-1} (1.2C) in the case of pure Fe_3O_4 electrode. These results demonstrate the better reaction reversibility of the composite electrode and thus shows improved electrochemical performance. To understand the microstructure evolution of the Fe_3O_4/C composite electrode, TEM images of the composite after 100 cycles are provided, as shown in Figure 8. It is clear that the composite almost retains the original morphology. Moreover, the nanocrystals after cycling are still well dispersed in the carbon matrix with no obvious agglomeration. Also, no structure damage is found. This further demonstrates that the remarkable cycling ability is primarily dependent on the constructed foamlike structure of the composite.

The electrode kinetics, as an important index for insight into the electrochemical behavior, was studied by electrochemical impedance spectroscopy (EIS) measurements (Figure 9). Generally, the impedance spectra are composed of a semicircle at middle-high frequency and a straight sloping line at low frequency. Here the intercept at the real axis of impedance (Z') reflects the total ohmic resistance of electrolyte and electrical contacts (R_e). The depressed semicircle in the middle frequency range indicates the charge transfer resistance (R_{ct}). The sloping line in the low frequency region represents the Warburg impedance (Z_w) associated with lithium ion diffusion in the solid phase. The kinetic data of Fe_3O_4 and Fe_3O_4/C composite electrodes are listed in Table 1.

No distinct difference exists in the R_e values of all samples, indicating that these cells work under consistent conditions. Apparently, the charge transfer resistance (R_{ct}) of the Fe_3O_4/C composite electrode is significantly smaller than that of the Fe_3O_4 electrode. This means rapid electron transfer during the electrochemical reaction of the composite. For the Fe_3O_4/C composite electrode, the resistance R_{ct} slightly decreases with cycling because of more sufficient contact between active materials and the electrolyte in this case. On the contrary, the resistance R_{ct} of bare Fe_3O_4 electrodes decreases after five cycles due to the electrode activation, while it increases dramatically after 100 cycles. This phenomenon may be

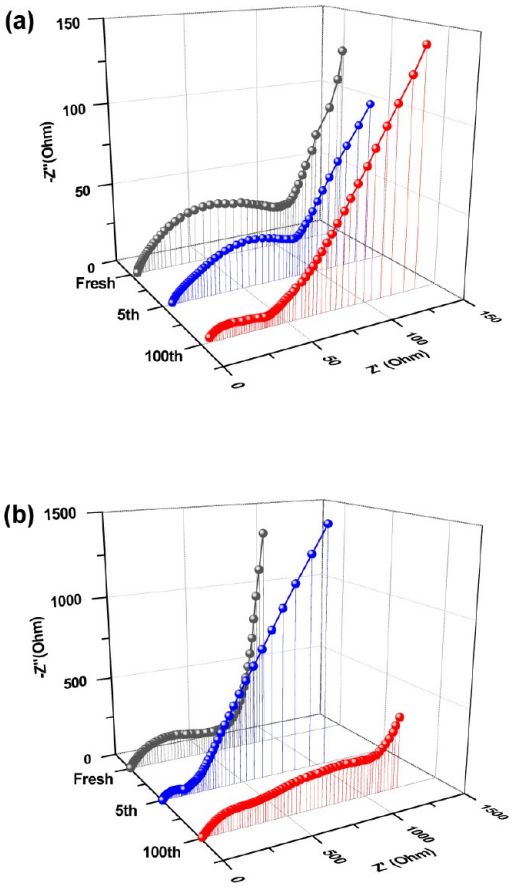

Figure 9. Nyquist plots of (a) Fe_3O_4/C composite electrodes and (b) bare Fe_3O_4 electrodes at selected cycles.

Table 1. Kinetic Parameters of the Fe_3O_4/C Composite and Fe_3O_4 Based on Modeling EIS Impendence Spectra

electrode	cycle number	R_e (Ω)	R_{ct} (Ω)	i_0 (A cm^{-2})
Fe_3O_4/C	fresh	3.968	100.9	3.18×10^{-5}
Fe_3O_4/C	5	4.93	63.71	5.04×10^{-5}
Fe_3O_4/C	100	4.0726	40.76	7.88×10^{-5}
Fe_3O_4	fresh	3.738	557.3	5.76×10^{-6}
Fe_3O_4	5	3.542	136.9	2.35×10^{-5}
Fe_3O_4	100	3.9582	1323.6	2.43×10^{-6}

ascribed to electrode degradation after long cycles of lithiation/delithiation. In addition, the exchange current densities are calculated, according to the following equation:[53−55]

$$i_0 = RT/nFR_{ct}$$

where R is the gas constant, T is the absolute temperature, n is the number of transferred electrons, and F is the Faraday constant. In the case of the Fe_3O_4/C electrode, the value of i_0 is much higher than that of the Fe_3O_4 electrode, which further indicates good reaction kinetics in the composite electrode. The foamlike composite presents satisfying electrochemical kinetics properties, leading to a remarkable improvement in rate performance.

CONCLUSIONS

The foamlike Fe_3O_4/C composite with porous architecture was successfully synthesized as a long cycle life anode for LIB by a self-expanding process. The reasons for its excellent electrochemical performance can be attributed to the following points: first, the designed structure effectively confines active seed growth and mitigates particle agglomeration. The nanosized Fe_3O_4 is beneficial to the enlargement of electrolyte contact area and the shortening of lithium ion diffusion path. Second, foamlike structure of the composite with a highly developed porous property is favorable for the electrolyte accessibility. Third, the three-dimensional (3D) conducting host is prone to promote charge transfer and improve the kinetic properties of the composite. As a result, the Fe_3O_4/C composite displays an outstanding cycle performance with a reversible capacity of 1008 mA h g^{-1} even up to 400 cycles at 0.2C, as well as a high rate capacity of 660 and 580 mA h g^{-1} at 3C and 5C, respectively.

AUTHOR INFORMATION

Corresponding Author

*E-mail: mudb@bit.edu.cn.

Notes

The authors declare no competing financial interest.

ACKNOWLEDGMENTS

This work was financially supported by the National 863 Program (2013AA050903) of China, Beijing Key Laboratory of Environmental Science and Engineering (20131039031).

REFERENCES

(1) Arico, A. S.; Bruce, P.; Scrosati, B.; Tarascon, J. M.; Van Schalkwijk, W. Nanostructured Materials for Advanced Energy Conversion and Storage Devices. *Nat. Mater.* **2005**, *4*, 366−377.

(2) Armand, M.; Tarascon, J. M. Building Better Batteries. *Nature* **2008**, *451*, 652−657.

(3) Amine, K.; Belharouak, I.; Chen, Z. H.; Tran, T.; Yumoto, H.; Ota, N.; Myung, S. T.; Sun, Y. K. Nanostructured Anode Material for High-Power Battery System in Electric Vehicles. *Adv. Mater.* **2010**, *22*, 3052−3057.

(4) Guo, B. K.; Wang, X. Q.; Fulvio, P. F.; Chi, M. F.; Mahurin, S. M.; Sun, X. G.; Dai, S. Soft-Templated Mesoporous Carbon-Carbon Nanotube Composites for High Performance Lithium-Ion Batteries. *Adv. Mater.* **2011**, *23*, 4661−4666.

(5) Shen, L. F.; Uchaker, E.; Yuan, C. Z.; Nie, P.; Zhang, M.; Zhang, X. G.; Cao, G. Z. Three-Dimensional Coherent Titania-Mesoporous Carbon Nanocomposite and Its Lithium-Ion Storage Properties. *ACS Appl. Mater. Interfaces* **2012**, *4*, 2985−2992.

(6) Taberna, P. L.; Mitra, S.; Poizot, P.; Simon, P.; Tarascon, J. M. High Rate Capabilities Fe_3O_4-Based Cu Nano-Architectured Electrodes for Lithium-Ion Battery Applications. *Nat. Mater.* **2006**, *5*, 567−573.

(7) Poizot, P.; Laruelle, S.; Grugeon, S.; Dupont, L.; Tarascon, J. M. Nano-Sized Transition-Metal Oxides as Negative-Electrode Materials for Lithium-Ion Batteries. *Nature* **2000**, *407*, 496−499.

(8) Guo, Y. G.; Hu, J. S.; Wan, L. J. Nanostructured Materials for Electrochemical Energy Conversion and Storage Devices. *Adv. Mater.* **2008**, *20*, 2878−2887.

(9) Wu, H.; Du, N.; Wang, J. Z.; Zhang, H.; Yang, D. R. Three-Dimensionally Porous Fe_3O_4 as High-Performance Anode Materials for Lithium-Ion Batteries. *J. Power Sources* **2014**, *246*, 198−203.

(10) Wang, P.; Gao, M. X.; Pan, H. G.; Zhang, J. L.; Liang, C.; Wang, J. H.; Zhou, P.; Liu, Y. F. A Facile Synthesis of Fe_3O_4/C Composite with High Cycle Stability as Anode Material for Lithium-Ion Batteries. *J. Power Sources* **2013**, *239*, 466−474.

(11) Lee, S. H.; Yu, S. H.; Lee, J. E.; Jin, A. H.; Lee, D. J.; Lee, N.; Jo, H.; Shin, K.; Ahn, T. Y.; Kim, Y. W.; Choe, H.; Sung, Y. E.; Hyeon, T. Self-Assembled Fe_3O_4 Nanoparticle Clusters as High-Performance Anodes for Lithium Ion Batteries via Geometric Confinement. *Nano Lett.* **2013**, *13*, 4249−4256.

(12) Zhou, Q.; Zhao, Z. B.; Wang, Z. Y.; Dong, Y. F.; Wang, X. Z.; Gogotsi, Y.; Qiu, J. S. Low Temperature Plasma Synthesis of Mesoporous Fe_3O_4 Nanorods Grafted on Reduced Graphene Oxide for High Performance Lithium Storage. *Nanoscale* **2014**, *6*, 2286−2291.
(13) Muraliganth, T.; Murugan, A. V.; Manthiram, A. Facile Synthesis of Carbon-Decorated Single-Crystalline Fe_3O_4 Nanowires and Their Application as High Performance Anode in Lithium Ion Batteries. *Chem. Commun.* **2009**, *47*, 7360−7362.
(14) Wang, L. L.; Liang, J. W.; Zhu, Y. C.; Mei, T.; Zhang, X.; Yang, Q.; Qian, Y. T. Synthesis of Fe_3O_4@C Core−Shell Nanorings and Their Enhanced Electrochemical Performance for Lithium-Ion Batteries. *Nanoscale* **2013**, *5*, 3627−3631.
(15) Li, D.; Qin, Q.; Duan, X. C.; Yang, J. Q.; Guo, W.; Zheng, W. J. General One-Pot Template-Free Hydrothermal Method to Metal Oxide Hollow Spheres and Their Photocatalytic Activities and Lithium Storage Properties. *ACS Appl. Mater. Interfaces* **2013**, *5*, 9095−9100.
(16) Luo, J. S.; Liu, J. L.; Zeng, Z. Y.; Ng, C. F.; Ma, L. J.; Zhang, H.; Lin, J. Y.; Shen, Z. X.; Fan, H. J. Three-Dimensional Graphene Foam Supported Fe_3O_4 Lithium Battery Anodes with Long Cycle Life and High Rate Capability. *Nano Lett.* **2013**, *13*, 6136−6143.
(17) Cao, Z. Y.; Wei, B. Q. High Rate Capability of Hydrogen Annealed Iron Oxide−Single Walled Carbon Nanotube Hybrid Films for Lithium-Ion Batteries. *ACS Appl. Mater. Interfaces* **2013**, *5*, 10246−10252.
(18) Lang, L. M.; Xu, Z. In Situ Synthesis of Porous Fe_3O_4/C Microbelts and Their Enhanced Electrochemical Performance for Lithium-Ion Batteries. *ACS Appl. Mater. Interfaces* **2013**, *5*, 1698−1703.
(19) Su, L. W.; Zhong, Y. R.; Zhou, Z. Role of Transition Metal Nanoparticles in Extra Lithium Storage Capacity of Transition Metal Oxides: A Case Study of Hierarchical Core-Shell Fe_3O_4@C and Fe@C Microspheres. *J. Mater. Chem. A* **2013**, *1*, 15158−15166.
(20) Lei, C.; Han, F.; Li, D.; Li, W. C.; Sun, Q.; Zhang, X. Q.; Lu, A. H. Dopamine as the Coating Agent and Carbon Precursor for the Fabrication of N-Doped Carbon Coated Fe_3O_4 Composites as Superior Lithium Ion Anodes. *Nanoscale* **2013**, *5*, 1168−1175.
(21) Chen, Y.; Song, B. H.; Li, M.; Lu, L.; Xue, J. M. Fe_3O_4 Nanoparticles Embedded in Uniform Mesoporous Carbon Spheres for Superior High-Rate Battery Applications. *Adv. Funct. Mater.* **2014**, *24*, 319−326.
(22) Wu, S.; Wang, Z. Y.; He, C. N.; Zhao, N. Q.; Shi, C. S.; Liu, E. Z.; Li, J. J. Synthesis of Uniform and Superparamagnetic Fe_3O_4 Nanocrystals Embedded in a Porous Carbon Matrix for a Superior Lithium Ion Battery Anode. *J. Mater. Chem. A* **2013**, *1*, 11011−11018.
(23) Li, D.; Li, X. W.; Wang, S. Y.; Zheng, Y. X.; Qiao, L.; He, D. Y. Carbon-Wrapped Fe_3O_4 Nanoparticle Films Grown on Nickel Foam as Binder-Free Anodes for High-Rate and Long-Life Lithium Storage. *ACS Appl. Mater. Interfaces* **2014**, *6*, 648−654.
(24) Wei, W.; Yang, S. B.; Zhou, H. X.; Lieberwirth, I.; Feng, X. L.; Müllen, K. 3D Graphene Foams Cross-Linked with Pre-Encapsulated Fe_3O_4 Nanospheres for Enhanced Lithium Storage. *Adv. Mater.* **2013**, *25*, 2909−2914.
(25) Cheng, J. L.; Wang, B.; Park, C. M.; Wu, Y. P.; Huang, H.; Nie, F. D. CNT@Fe_3O_4@C Coaxial Nanocables: One-Pot, Additive-Free Synthesis and Remarkable Lithium Storage Behavior. *Chem.—Eur. J.* **2013**, *19*, 9866−9874.
(26) Kang, E.; Jung, Y. S.; Cavanagh, A. S.; Kim, G. H.; George, S. M.; Dillon, A. C.; Kim, J. K.; Lee, J. Fe_3O_4 Nanoparticles Confined in Mesocellular Carbon Foam for High Performance Anode Materials for Lithium-Ion Batteries. *Adv. Funct. Mater.* **2011**, *21*, 2430−2438.
(27) Yoon, T.; Chae, C.; Sun, Y. K.; Zhao, X.; Kung, H. H.; Lee, J. K. Bottom-Up In Situ Formation of Fe_3O_4 Nanocrystals in a Porous Carbon Foam for Lithium-Ion Battery Anodes. *J. Mater. Chem.* **2011**, *21*, 17325−17330.
(28) Wu, F.; Huang, R.; Mu, D. B.; Shen, X. Y.; Wu, B. R. A Novel Composite with Highly Dispersed Fe_3O_4 Nanocrystals on Ordered Mesoporous Carbon as an Anode for Lithium Ion Batteries. *J. Alloys Compd.* **2014**, *585*, 783−789.
(29) Chen, L. Y.; Lin, Z.; Zhao, C. L.; Zheng, Y. Y.; Zhou, Y.; Peng, H. Direct Synthesis and Characterization of Mesoporous Fe_3O_4 Through Pyrolysis of Ferric Nitrate-Ethylene Glycol Gel. *J. Alloys Compd.* **2011**, *509*, L1−L5.
(30) Schnepp, Z.; Wimbush, S. C.; Antonietti, M.; Giordano, C. Synthesis of Highly Magnetic Iron Carbide Nanoparticles via a Biopolymer Route. *Chem. Mater.* **2010**, *22*, 5340−5344.
(31) Schnepp, Z.; Thomas, M.; Glatzel, S.; Schlichte, K.; Palkovits, R.; Giordano, C. One Pot Route to Sponge-Like Fe_3N Nanostructures. *J. Mater. Chem.* **2011**, *21*, 17760−17764.
(32) Schnepp, Z. Biopolymers as a Flexible Resource for Nanochemistry. *Angew. Chem., Int. Ed.* **2013**, *52*, 1096−1108.
(33) Schnepp, Z.; Wimbush, S. C.; Mann, S.; Hall, S. R. Alginate-Mediated Routes to the Selective Synthesis of Complex Metal Oxide Nanostructures. *CrystEngComm* **2010**, *12*, 1410−1415.
(34) Su, D. W.; Ahn, H. J.; Wang, G. X. One-Dimensional Magnetite Fe_3O_4 Nanowires as Electrode Material for Li-Ion Batteries with Improved Electrochemical Performance. *J. Power Sources* **2013**, *244*, 742−746.
(35) Zeng, Z. P.; Zhao, H. L.; Wang, J.; Lv, P. P.; Zhang, T. H.; Xia, Q. Nanostructured Fe_3O_4@C as Anode Material for Lithium-Ion Batteries. *J. Power Sources* **2014**, *248*, 15−21.
(36) Mao, Y.; Duan, H.; Xu, B.; Zhang, L.; Hu, Y. S.; Zhao, C. C.; Wang, Z. X.; Chen, L. Q.; Yang, Y. S. Lithium Storage in Nitrogen-Rich Mesoporous Carbon Materials. *Energy Environ. Sci.* **2012**, *5*, 7950−7955.
(37) Chen, X. Y.; Chen, C.; Zhang, Z. J.; Xie, D. H. Gelatin-Derived Nitrogen-Doped Porous Carbon via a Dual-Template Carbonization Method for High Performance Supercapacitors. *J. Mater. Chem. A* **2013**, *1*, 10903−10911.
(38) Mane, G. P.; Talapaneni, S. N.; Anand, C.; Varghese, S.; Lwai, H.; Ji, Q. M.; Ariga, K.; Mori, T.; Vinu, A. Preparation of Highly Ordered Nitrogen-Containing Mesoporous Carbon from a Gelatin Biomolecule and Its Excellent Sensing of Acetic Acid. *Adv. Funct. Mater.* **2012**, *22*, 3596−3604.
(39) Xu, B.; Hou, S. S.; Cao, G. P.; Wu, F.; Yang, Y. S. Sustainable Nitrogen-Doped Porous Carbon with High Surface Areas Prepared from Gelatin for Supercapacitors. *J. Mater. Chem.* **2012**, *22*, 19088−19093.
(40) He, C. N.; Wu, S.; Zhao, N. Q.; Shi, C. S.; Liu, E. Z.; Li, J. J. Carbon-Encapsulated Fe_3O_4 Nanoparticles as a High-Rate Lithium Ion Battery Anode Material. *ACS Nano* **2013**, *7*, 4459−4469.
(41) Zhao, N. Q.; Wu, S.; He, C. N.; Wang, Z. Y.; Shi, C. S.; Liu, E. Z.; Li, J. J. One-Pot Synthesis of Uniform Fe_3O_4 Nanocrystals Encapsulated in Interconnected Carbon Nanospheres for Superior Lithium Storage Capability. *Carbon* **2013**, *57*, 130−138.
(42) Ming, H.; Ming, J.; Li, X. W.; Zhou, Q.; Jin, L. L.; Fu, Y.; Adkins, J.; Kang, Z. H.; Zheng, J. W. Synthesis of N-Doped Carbon Coated Metal Oxide Nanoparticles for Enhanced Li-Ion Storage Ability. *RSC Adv.* **2013**, *3*, 15613−15617.
(43) Meng, Q. N.; Zhang, F. F.; Wang, L. M.; Xiang, S. Y.; Zhu, S. J.; Zhang, G. Y.; Zhang, K.; Yang, B. Facile Fabrication of Mesoporous N-Doped Fe_3O_4@C Nanospheres as Superior Anodes for Li-Ion Batteries. *RSC Adv.* **2014**, *4*, 713−716.
(44) Chang, Y. H.; Li, J.; Wang, B.; Luo, H.; He, H. Y.; Song, Q.; Zhi, L. J. Synthesis of 3D Nitrogen-Doped Graphene/Fe_3O_4 by a Metal Ion Induced Self-Assembly Process for High-Performance Li-Ion Batteries. *J. Mater. Chem. A* **2013**, *1*, 14658−14665.
(45) Ding, Z. J.; Zhao, L.; Suo, L. M.; Jiao, Y.; Meng, S.; Hu, Y. S.; Wang, Z. X.; Chen, L. Q. Towards Understanding the Effects of Carbon and Nitrogen-Doped Carbon Coating on the Electrochemical Performance of $Li_4Ti_5O_{12}$ in Lithium Ion Batteries: A Combined Experimental and Theoretical Study. *Phys. Chem. Chem. Phys.* **2011**, *13*, 15127−15133.
(46) Wang, L.; Zheng, Y. L.; Wang, X. H.; Chen, S. H.; Xu, F. G.; Zou, L.; Wu, J. F.; Sun, L. L.; Li, Z.; Hou, H. Q.; Song, Y. H. Nitrogen-Doped Porous Carbon/Co_3O_4 Nanocomposites as Anode Materials for Lithium-Ion Batteries. *ACS Appl. Mater. Interfaces* **2014**, *6*, 7117−7125.

(47) Meng, X. B.; Zhong, Y.; Sun, Y. F.; Banis, M. N.; Li, R. Y.; Sun, X. L. Nitrogen-Doped Carbon Nanotubes Coated by Atomic Layer Deposited SnO_2 with Controlled Morphology and Phase. *Carbon* **2011**, *49*, 1133−1144.
(48) Zhu, X.; Song, X. Y.; Ma, X. L.; Ning, G. Q. Enhanced Electrode Performance of Fe_2O_3 Nanoparticle-Decorated Nanomesh Graphene as Anodes for Lithium-Ion Batteries. *ACS Appl. Mater. Interfaces* **2014**, *6*, 7189−7197.
(49) Lim, H. S.; Sun, Y. K.; Suh, K. D. Rattle Type α-Fe_2O_3 Submicron Spheres with a Thin Carbon Layer for Lithium-Ion Battery Anodes. *J. Mater. Chem. A* **2013**, *1*, 10107−10111.
(50) Xiao, Y.; Wang, X.; Wang, W.; Zhao, D.; Cao, M. H. Engineering Hybrid between MnO and N-Doped Carbon to Achieve Exceptionally High Capacity for Lithium-Ion Battery Anode. *ACS Appl. Mater. Interfaces* **2014**, *6*, 2051−2058.
(51) Wang, R. H.; Xu, C. H.; Sun, J.; Gao, L.; Yao, H. L. Solvothermal-Induced 3D Macroscopic SnO_2/Nitrogen-Doped Graphene Aerogels for High Capacity and Long-Life Lithium Storage. *ACS Appl. Mater. Interfaces* **2014**, *6*, 3427−3436.
(52) Hou, X. J.; Wang, X. F.; Liu, B.; Wang, Q. F.; Luo, T.; Chen, D.; Shen, G. Z. Hierarchical $MnCo_2O_4$ Nanosheet Arrays/Carbon Cloths as Integrated Anodes for Lithium-Ion Batteries with Improved Performance. *Nanoscale* **2014**, *6*, 8858−8864.
(53) Wang, X. Y.; Hao, H.; Liu, J. L.; Huang, T.; Yu, A. S. A Novel Method for Preparation of Macroposous Lithium Nickel Manganese Oxygen as Cathode Material for Lithium Ion Batteries. *Electrochim. Acta* **2011**, *56*, 4065−4069.
(54) Liu, H.; Wang, G. X.; Liu, J.; Qiao, S. Z.; Ahn, H. Highly Ordered Mesoporous NiO Anode Material for Lithium Ion Batteries with an Excellent Electrochemical Performance. *J. Mater. Chem.* **2011**, *21*, 3046−3052.
(55) Shen, X. Y.; Mu, D. B.; Chen, S.; Wu, B. R.; Wu, F. Enhanced Electrochemical Performance of ZnO-Loaded/Porous Carbon Composite as Anode Materials for Lithium Ion Batteries. *ACS Appl. Mater. Interfaces* **2013**, *5*, 3118−3125.

■ NOTE ADDED AFTER ASAP PUBLICATION

This paper was published on the Web on October 20, 2014, with incorrect units for frequency ranges in the Experimental Section. The corrected version was reposted on October 24, 2014.